Supporting Information for "Rift Focussing and Magmatism During Late-Stage Rifting in Afar, Ethiopia"

C. Moore[1], T. Wright[1], A. Hooper[1]

[1]COMET, School of Earth and Environment, University of Leeds, Leeds, LS2 9JT, UK

Contents of this file

1. Time Series Methodology
2. Table S1
3. Figures S1 - S7

Corresponding author: Chris Moore, COMET, School of Earth and Environment, University of Leeds, Leeds, LS2 9JT, UK (ee12cm@leeds.ac.uk)

Time Series Methodology

Our SBAS style and time series methodology from unwrapped interferograms to 3D (rift-perpendicular, rift-parallel, vertical) average velocities consists of the following steps:

1. Invert each pixel for a LOS displacement time series using an SBAS style least-squares inversion as shown in Equation 2 for a network of 5 interferograms (i_{01}, i_{02}, i_{12}, i_{13}, i_{23}) covering 4 epochs (d_0, d_1, d_2, d_3) with zero displacement at the first epoch ($d_0 = 0$). We perform this inversion at each pixel in the frame using all available coherent interferograms, rejecting pixels where the interferogram network at any epoch is disconnected.

$$\begin{bmatrix} i_{01} \\ i_{02} \\ i_{12} \\ i_{13} \\ i_{23} \end{bmatrix} = \begin{bmatrix} 1 & 0 & 0 \\ 0 & 1 & 0 \\ -1 & 1 & 0 \\ -1 & 0 & 1 \\ 0 & -1 & 1 \end{bmatrix} \begin{bmatrix} d_1 & d_2 & d_3 \end{bmatrix} \tag{2}$$

2. Estimate the error in the time series using the RMS misfit.

(i) Filter the displacement time series at each pixel using a Laplacian filter with a temporal width of 3 epochs with a scaling factor (K) of 3 (see Equation 3 for a time series of unfiltered displacements (d_0, d_1, d_2, d_3), filtered displacements (f_0, f_1, f_2, f_3) and the time gaps between epochs (t_{01}, t_{12}, t_{23}).

$$\begin{bmatrix} d_0 \\ d_1 \\ d_2 \\ d_3 \end{bmatrix} = K \begin{bmatrix} 1/K & 0 & 0 & 0 \\ -t_{01} & t_{01}+t_{12} & -t_{12} & 0 \\ 0 & -t_{12} & t_{12}+t_{23} & -t_{23} \\ 0 & 0 & 0 & 1/K \end{bmatrix} \begin{bmatrix} f_0 & f_1 & f_2 & f_3 \end{bmatrix} \tag{3}$$

(ii) For each pixel, we calculate the misfit of the unfiltered time series against the Laplacian filtered time series at every epoch ($m_{xyt} = d_{xyt} - f_{xyt}$).

(iii) Using Equation 4, we calculate the RMS misfit of each pixel (r_{xy}) using the time series of misfits (m_t), and the RMS misfit of each epoch (r_t) using the misfit of every pixel

(m_{xy}).

$$r = \sqrt{\frac{m_1^2 + m_2^2 + ...m_N^2}{N}} \tag{4}$$

(iv) To resolve an RMS misfit value for each pixel at every epoch (r_{xyt}), we scale the spatial RMS misfit map (r_{xy}) to the value of temporal RMS misfit at each epoch (r_t) using the RMS misfit of r_{xy}.

$$r_{xyt} = r_{xy} \frac{r_t}{\sqrt{\frac{r_{11}^2 + r_{12}^2 + r_{21}^2 + ...r_{NM}^2}{NM}}} \tag{5}$$

3. Calculate the APS and remove from the LOS displacement time series.

(i) Low-pass filter the time series of each pixel using a local linear trend with a fixed filter width of $\pm$ 0.5 years from the target epoch. The weighting of the epoch displacements is dependant on the temporal distance from the target epoch, the RMS misfit value, and outlier rejection. By editing the "smooth" function in Matlab, we convert the RMS misfit values into weights using the Bi-Square function (Cleveland & Devlin, 1988), where zero weight is given to RMS values that are $>$ 6 standard deviations of the local misfits.

(ii) Remove the low-pass filtered time series from the unfiltered data to create a high-pass filtered time series.

(iii) On the high-pass temporal filtered data, apply a low-pass spatial filter for each epoch using a Gaussian kernel with a half-width of $\sim$ 2 km to resolve the APS.

(iv) Remove the calculated APS from the displacement time series, and correct for any residual orbital or atmospheric errors by inverting for and removing planar ramps in space, and a linear trend of phase with elevation.

4. Calculate the average LOS velocity for each pixel from the time series of displacements (d_1, d_2, ... d_N, with time steps t_1, t_2, ... t_N) by inverting for the average displacement rate (v) and a constant offset (c, to allow the displacement at $t = 0$ to be non-zero). To resolve uncertainties in the average velocity estimates (Q_{mm}), we include a data VCM (Q_{dd}) by using the time series of RMS misfit values at each pixel (r_1, r_2, ... r_N) as independent error sources (see Equations 6-9).

$$Q_{dd} = \begin{bmatrix} r_1^2 & 0 & ... & 0 \\ 0 & r_2^2 & ... & 0 \\ ... & ... & ... & ... \\ 0 & 0 & ... & r_N^2 \end{bmatrix} \tag{6}$$

$$G = \begin{bmatrix} t_1 & 1 \\ t_2 & 1 \\ ... & ... \\ t_N & 1 \end{bmatrix} \tag{7}$$

$$Q_{mm} = (G^T Q_{dd}^{-1} G)^{-1} \tag{8}$$

$$\begin{bmatrix} v & c \end{bmatrix} = Q_{mm} G^T Q_{dd}^{-1} \begin{bmatrix} d_1 \\ d_2 \\ ... \\ d_N \end{bmatrix} \tag{9}$$

5. Connect the frame LOS velocity maps within their respective tracks.

(i) For each track, we sub-sample the frame velocity maps to 5×5 km in frame overlap regions, and 10×10 km elsewhere.

(ii) Keeping one frame in the track uncorrected, we reference the other frames to it by inverting for planar ramps in space for each frame such that the values in the frame overlap regions are equal. We then remove the ramps from the respective frames, and use the mean value in the frame overlap regions when combining the frames into a single track.

6. Reference the track LOS velocities to a stable Nubia GNSS reference frame.

(i) Convert the GNSS velocities in the east (E) and north (N) directions to rift-perpendicular ($H1$) and rift-parallel ($H2$) directions using Equation 10, using the orientation of the rift axis (α) of 151°N. Then interpolate smooth GNSS velocity fields in the rift-perpendicular and rift-parallel directions using the natural neighbour algorithm and the "griddata" function in Matlab.

$$\begin{bmatrix} E \\ N \end{bmatrix} = \begin{bmatrix} cos(\alpha) & -sin(\alpha) \\ sin(\alpha) & -cos(\alpha) \end{bmatrix} \begin{bmatrix} H1 & H2 \end{bmatrix} \tag{10}$$

(ii) After masking areas with surface deformation that is not related to the long-wavelength plate spreading (i.e. related to volcanic or anthropogenic activity), we subsample the track velocities to 5×5 km in track overlap regions, and 10×10 km elsewhere.

(iii) Using the points where there are ascending, descending, and interpolated GNSS data, we invert for 3D velocities (rift-perpendicular, rift-parallel, vertical, see Equation 1 (main text)) and a quadratic function for each track. We then remove the quadratic function from each track to resolve LOS velocities referenced to stable Nubia.

7. Resolve 3D velocities (rift-perpendicular, rift-parallel, vertical) at each pixel (see Equation 1 (main text)), using the smooth GNSS rift-parallel velocity field to help constrain the inversion (e.g. Weiss et al., 2020), and uncertainties in LOS velocity as independent errors in a VCM (as shown in Equation 6).

References

Bagnardi, M., & Hooper, A. (2018). Inversion of Surface Deformation Data for Rapid Estimates of Source Parameters and Uncertainties: A Bayesian Approach. *Geochemistry, Geophysics, Geosystems*, *19*. doi: 10.1029/2018GC007585

Cleveland, W. S., & Devlin, S. J. (1988). Locally weighted regression: an approach to

regression analysis by local fitting. *Journal of the American statistical association*, *83*(403), 596–610.

King, R., Floyd, M., Reilinger, R., & Bendick, R. (2019). GPS velocity field (MIT 2019.0) for the East African Rift System generated by King et al.. Interdisciplinary Earth Data Alliance (IEDA). *Accessed on 20 Sep 2019*.

Mogi, K. (1958). Relations between the Eruptions of Various Volcanoes and the Defomormations of the Ground Surfaces around them. *Bulletin of the Earthquake Research Institute*, *36*, 99–134.

Okada, Y. (1985). Surface deformation due to shear and tensile faults in a half-space. *Bulletin of the seismological society of America*, *75*(4), 1135–1154.

Weiss, J. R., Walters, R. J., Morishita, Y., Wright, T. J., Lazecky, M., Wang, H., ... Parsons, B. (2020). High-resolution Surface Velocities and Strain for Anatolia from Sentinel-1 InSAR and GNSS Data. *EarthArXiv*.

Yu, C., Li, Z., & Penna, N. T. (2018). Interferometric synthetic aperture radar atmospheric correction using a GPS-based iterative tropospheric decomposition model. *Remote Sensing of Environment*, *204*, 109–121. doi: 10.1016/j.rse.2017.10.038

Yu, C., Penna, N. T., & Li, Z. (2017). Generation of real-time mode high-resolution water vapor fields from GPS observations. *Journal of Geophysical Research*, *122*(3), 2008–2025. doi: 10.1002/2016JD025753

Frame	Start Date	End Date	No. of IFGs
006D-07728-131313	11.11.2014	30.06.2019	198
006D-07929-131313	18.10.2014	17.08.2019	334
014A-07524-101303	23.11.2014	24.02.2019	85
014A-07688-131313	23.11.2014	18.07.2019	223
014A-07885-131313	30.10.2014	18.07.2019	187
079D-07503-061113	23.11.2015	10.08.2019	178
079D-07694-131313	23.10.2014	17.07.2019	337
079D-07894-131313	23.10.2014	17.07.2019	277
087A-07674-131313	11.10.2014	11.03.2017	92
087A-07889-131313	11.10.2014	11.03.2017	82
116A-07590-071313	13.10.2014	13.07.2019	316
116A-07768-131305	12.12.2014	13.07.2019	193

Table S1. Start date, end date (DD.MM.YYYY), and the number of interferograms (IFGs) used to build the displacement time series for each frame. Frame names are defined by the track (e.g. 006D for descending track 6), the frame ID (e.g. 07728), and the number of bursts in each of the 3 sub-swaths within the frame (e.g. 131313 for a maximum of 13 bursts in each sub-swath).

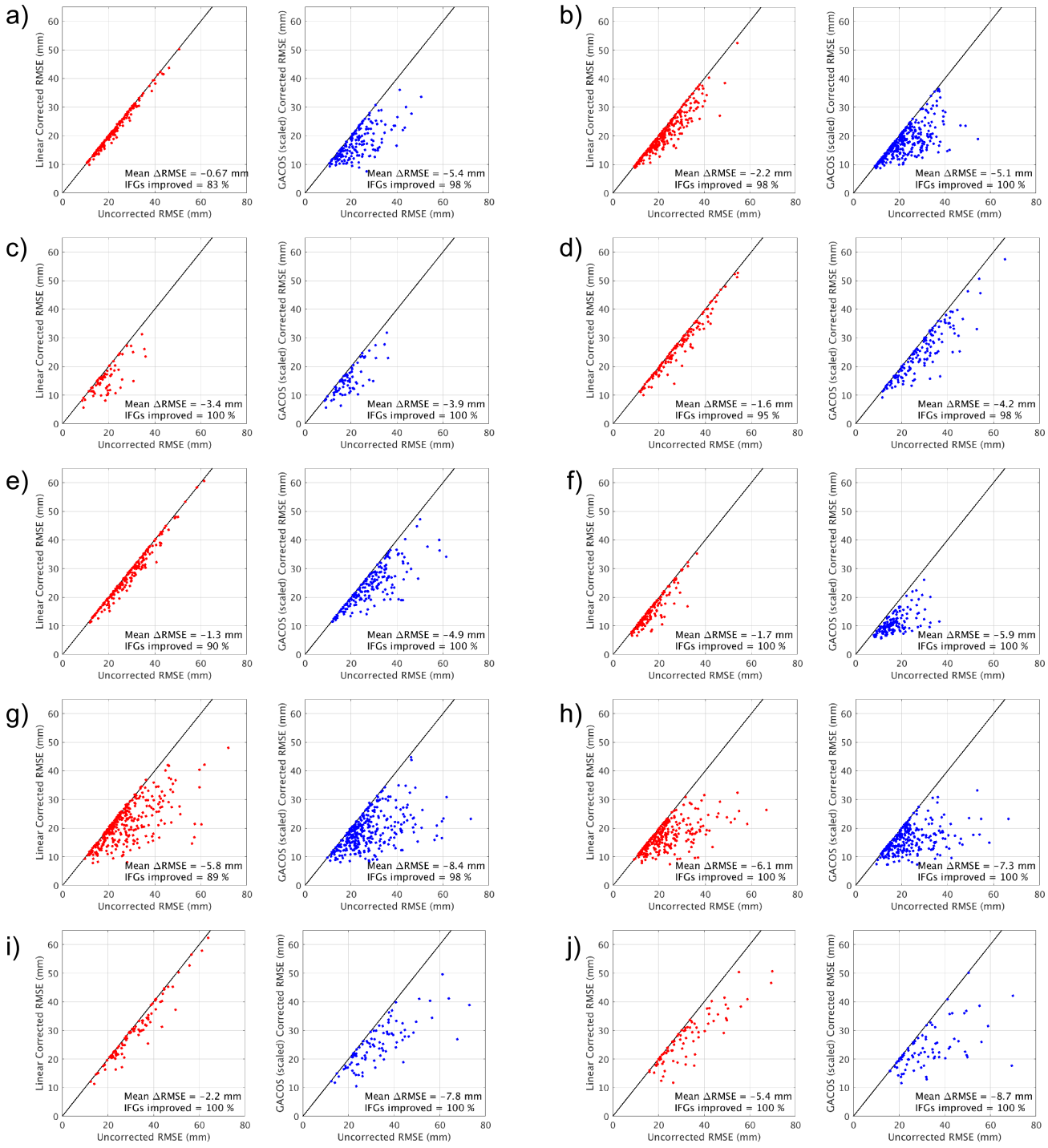
a)
Linear Corrected RMSE (mm)
Uncorrected RMSE (mm)
Mean ΔRMSE = −0.67 mm
IFGs improved = 83 %
GACOS (scaled) Corrected RMSE (mm)
Uncorrected RMSE (mm)
Mean ΔRMSE = −5.4 mm
IFGs improved = 98 %
b)
Linear Corrected RMSE (mm)
Uncorrected RMSE (mm)
Mean ΔRMSE = −2.2 mm
IFGs improved = 98 %
GACOS (scaled) Corrected RMSE (mm)
Uncorrected RMSE (mm)
Mean ΔRMSE = −5.1 mm
IFGs improved = 100 %
c)
Linear Corrected RMSE (mm)
Uncorrected RMSE (mm)
Mean ΔRMSE = −3.4 mm
IFGs improved = 100 %
GACOS (scaled) Corrected RMSE (mm)
Uncorrected RMSE (mm)
Mean ΔRMSE = −3.9 mm
IFGs improved = 100 %
d)
Linear Corrected RMSE (mm)
Uncorrected RMSE (mm)
Mean ΔRMSE = −1.6 mm
IFGs improved = 95 %
GACOS (scaled) Corrected RMSE (mm)
Uncorrected RMSE (mm)
Mean ΔRMSE = −4.2 mm
IFGs improved = 98 %
e)
Linear Corrected RMSE (mm)
Uncorrected RMSE (mm)
Mean ΔRMSE = −1.3 mm
IFGs improved = 90 %
GACOS (scaled) Corrected RMSE (mm)
Uncorrected RMSE (mm)
Mean ΔRMSE = −4.9 mm
IFGs improved = 100 %
f)
Linear Corrected RMSE (mm)
Uncorrected RMSE (mm)
Mean ΔRMSE = −1.7 mm
IFGs improved = 100 %
GACOS (scaled) Corrected RMSE (mm)
Uncorrected RMSE (mm)
Mean ΔRMSE = −5.9 mm
IFGs improved = 100 %
g)
Linear Corrected RMSE (mm)
Uncorrected RMSE (mm)
Mean ΔRMSE = −5.8 mm
IFGs improved = 89 %
GACOS (scaled) Corrected RMSE (mm)
Uncorrected RMSE (mm)
Mean ΔRMSE = −8.4 mm
IFGs improved = 98 %
h)
Linear Corrected RMSE (mm)
Uncorrected RMSE (mm)
Mean ΔRMSE = −6.1 mm
IFGs improved = 100 %
GACOS (scaled) Corrected RMSE (mm)
Uncorrected RMSE (mm)
Mean ΔRMSE = −7.3 mm
IFGs improved = 100 %
i)
Linear Corrected RMSE (mm)
Uncorrected RMSE (mm)
Mean ΔRMSE = −2.2 mm
IFGs improved = 100 %
GACOS (scaled) Corrected RMSE (mm)
Uncorrected RMSE (mm)
Mean ΔRMSE = −7.8 mm
IFGs improved = 100 %
j)
Linear Corrected RMSE (mm)
Uncorrected RMSE (mm)
Mean ΔRMSE = −5.4 mm
IFGs improved = 100 %
GACOS (scaled) Corrected RMSE (mm)
Uncorrected RMSE (mm)
Mean ΔRMSE = −8.7 mm
IFGs improved = 100 %

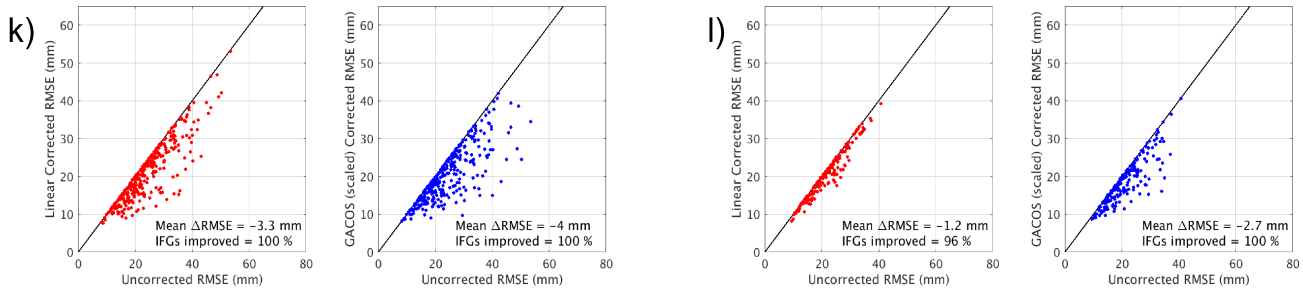

Figure S1. Residual root-mean-square error (RMSE) for all interferograms in each frame after applying atmospheric phase delay corrections using a linear correlation of phase with elevation (red), and a scaled GACOS atmospheric model (blue) (Yu et al., 2017, 2018). Also shown is the mean change in RMSE, and the percentage of interferograms where the RMSE was improved following the correction. Frames: (a) 006D-07728-131313, (b) 006D-07929-131313, (c) 014A-07524-101303, (d) 014A-07688-131313, (e) 014A-07885-131313, (f) 079D-07503-061113, (g) 079D-07694-131313, (h) 079D-07894-131313, (i) 087A-07674-131313, (j) 087A-07889-131313, (k) 116A-07590-071313, (l) 116A-07768-131305.

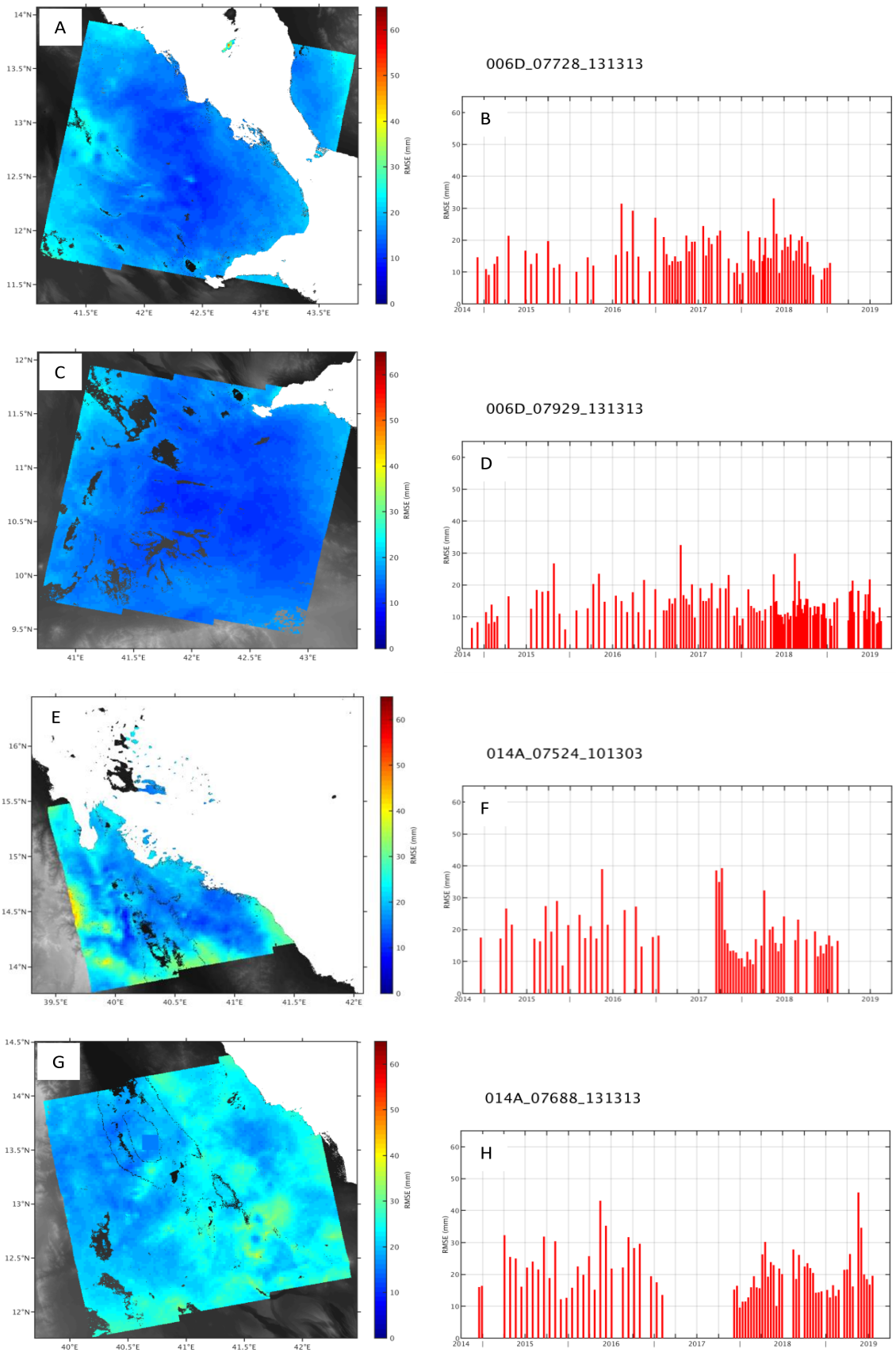
A
B
006D_07728_131313
C
D
006D_07929_131313
E
F
014A_07524_101303
G
H
014A_07688_131313
RMSE (mm)

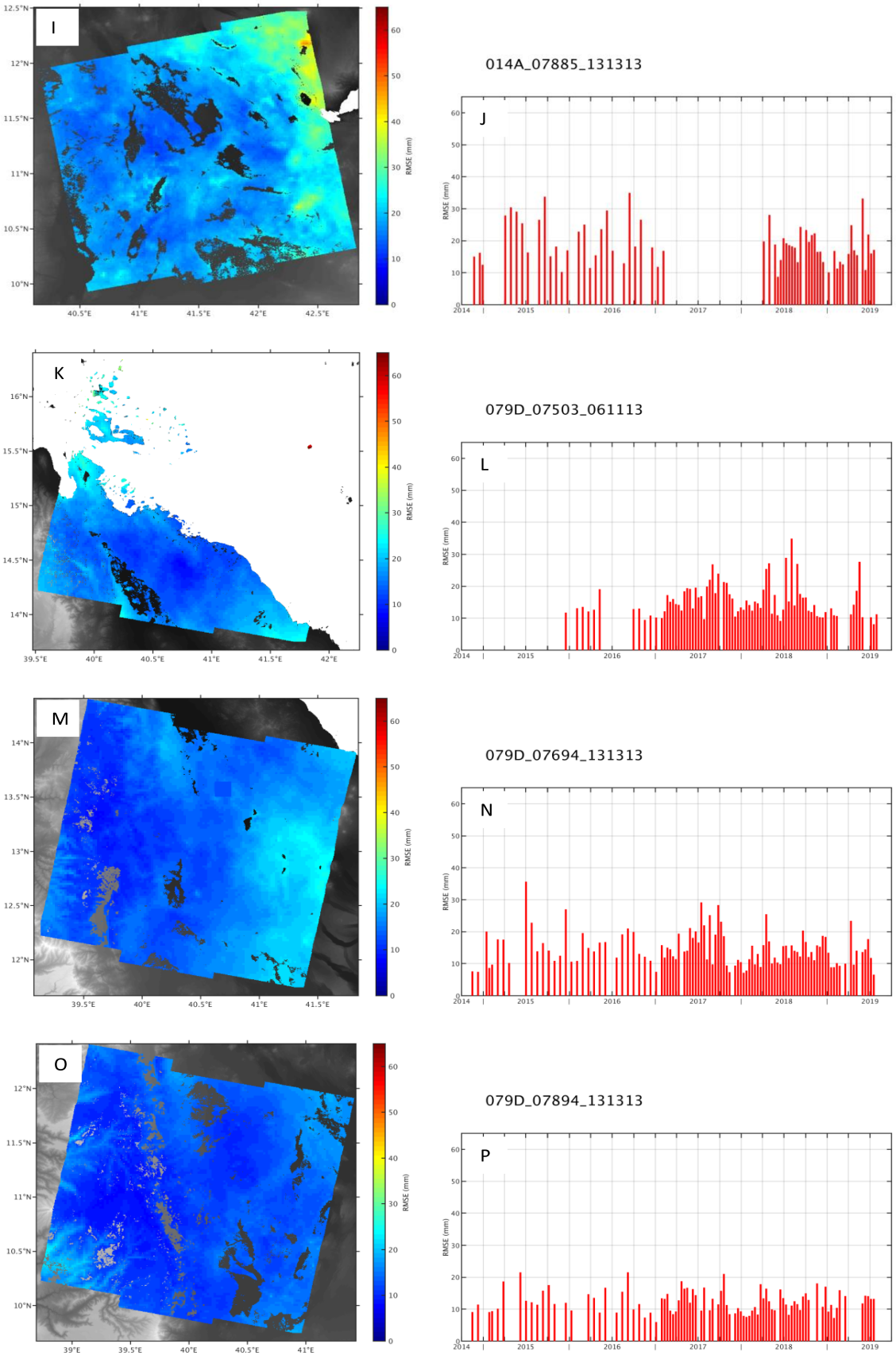
I
014A_07885_131313
J
K
079D_07503_061113
L
M
079D_07694_131313
N
O
079D_07894_131313
P
RMSE (mm)

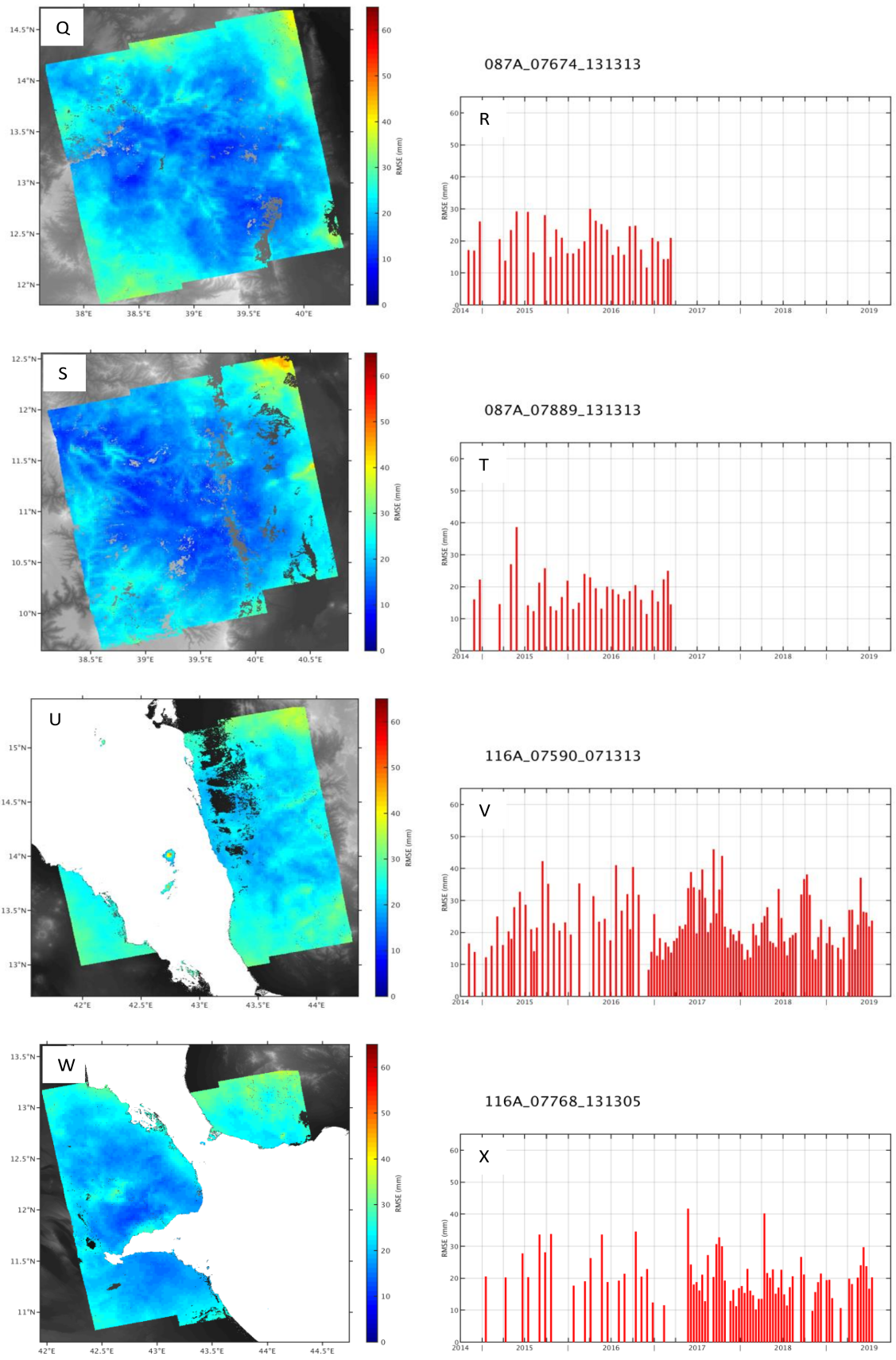
Q
087A_07674_131313
R
S
087A_07889_131313
T
U
116A_07590_071313
V
W
116A_07768_131305
X
RMSE (mm)

Figure S2. Frame root-mean-square error (RMSE) in space for each pixel (A,C,E,G,I,K,M,O,Q,S,U,W) and time for each epoch (B,D,F,H,J,L,N,P,R,T,V,X). Frames: (A,B) 006D-07728-131313, (C,D) 006D-07929-131313, (E,F) 014A-07524-101303, (G,H) 014A-07688-131313, (I,J) 014A-07885-131313, (K,L) 079D-07503-061113, (M,N) 079D-07694-131313, (O,P) 079D-07894-131313, (Q,R) 087A-07674-131313, (S,T) 087A-07889-131313, (U,V) 116A-07590-071313, (W,X) 116A-07768-131305.

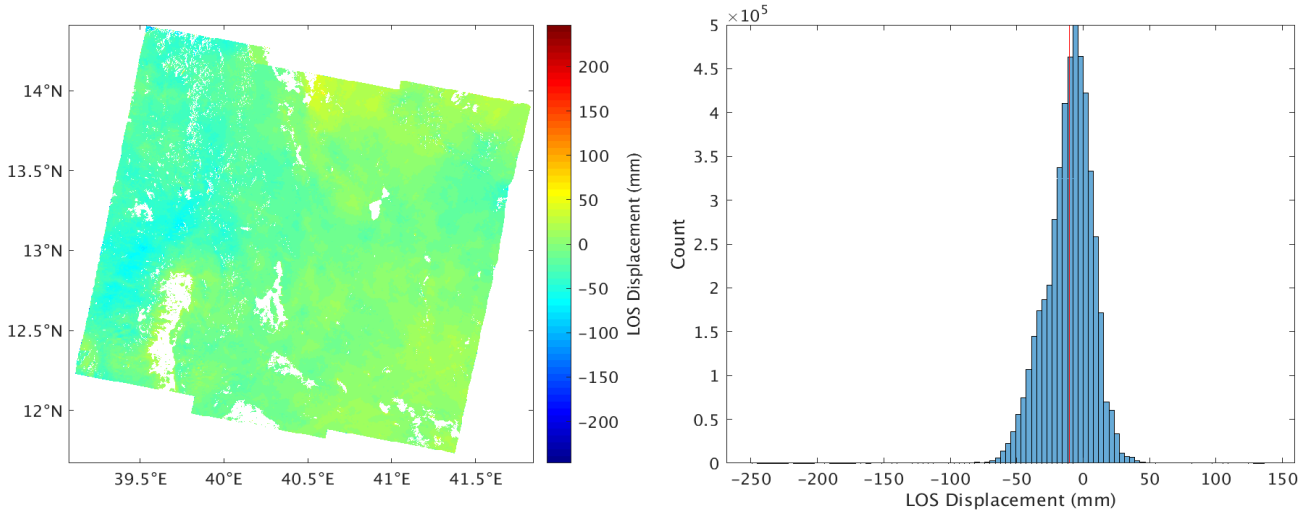

Figure S3. Demonstrating line of sight (LOS) displacement bias ('phase bias') from the difference between 12 and 24 day interferogram 'daisy-chain' stacks for frame 079D-07694-131313 between 06 December 2017 and 11 February 2019. Residuals shown in map view and as a histogram with the mean value indicated by a vertical red line.

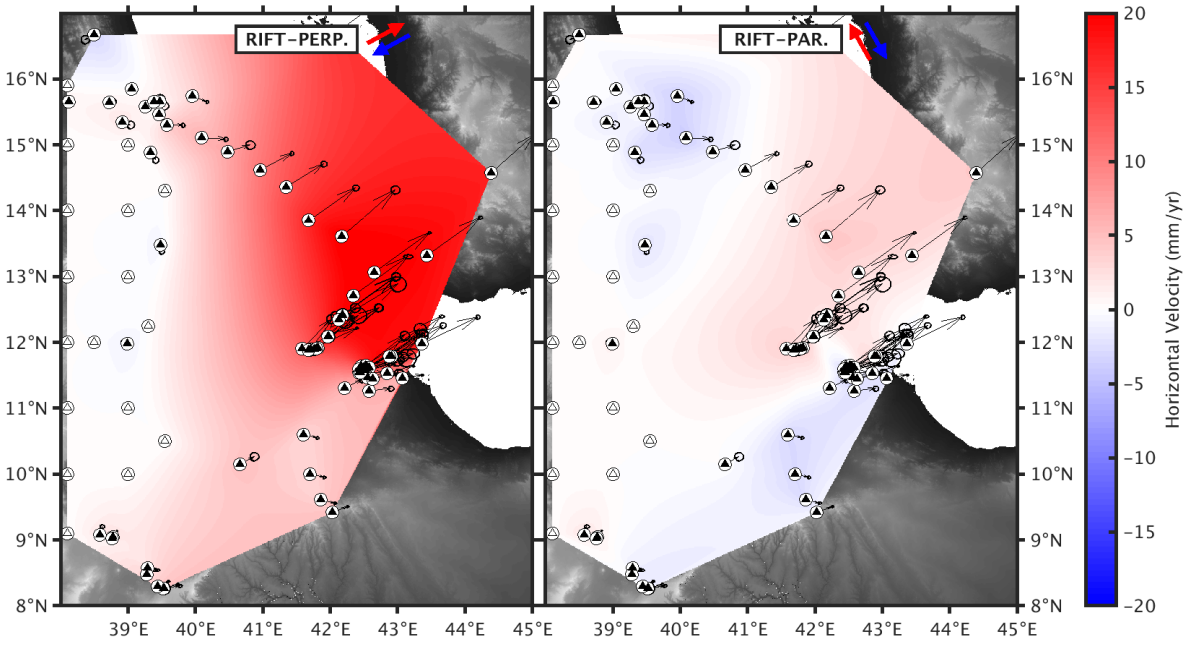

Figure S4. GNSS derived rift-perpendicular (positive towards 61°N) and rift-parallel (positive towards -29°N) horizontal velocity fields. Black triangles indicate the subset of GNSS stations used from (King et al., 2019) with velocity vectors and error ellipses White triangles indicate the synthetic stations with zero velocity on the stable Nubian plate used to help constrain the velocity fields.

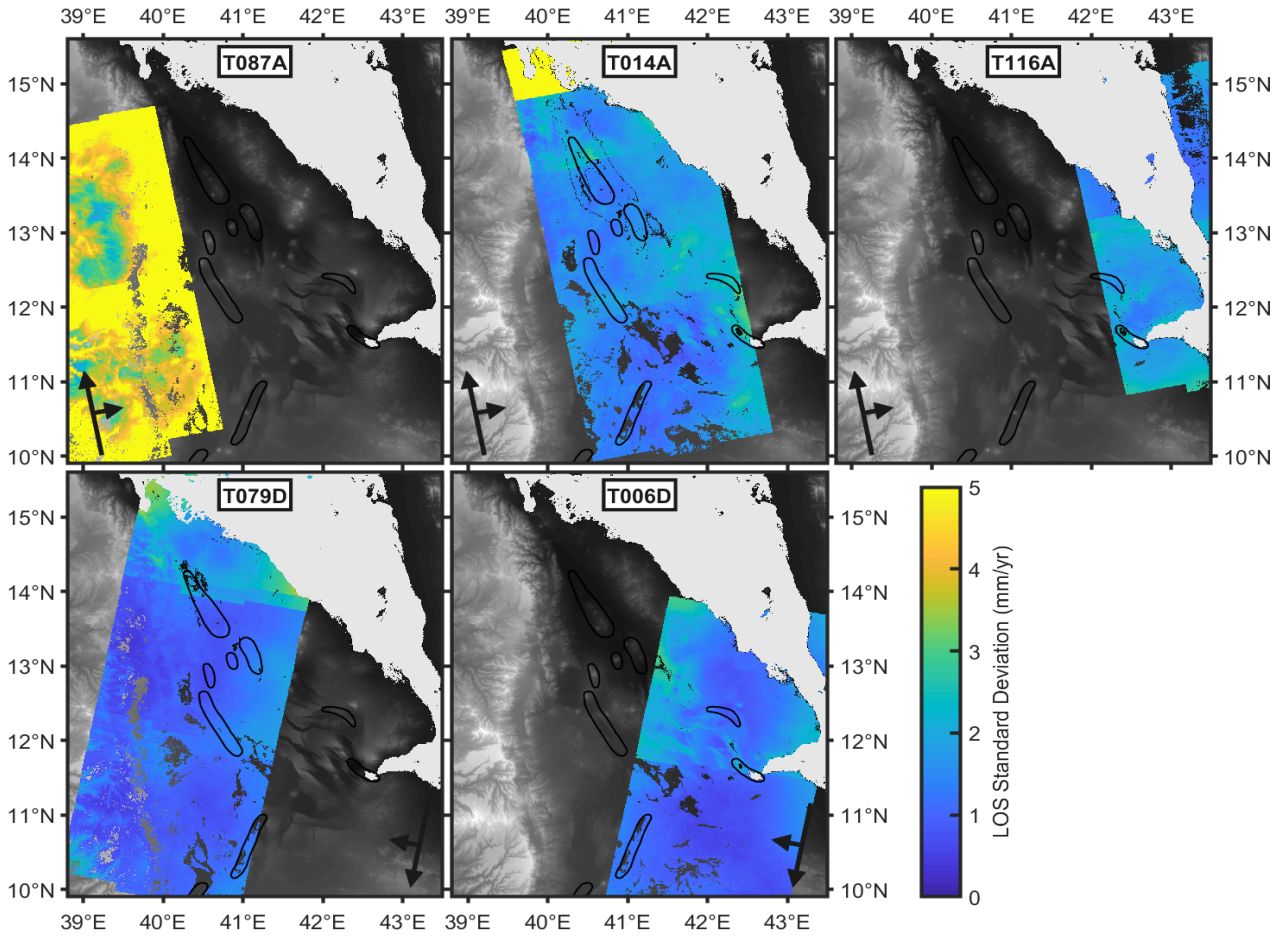

Figure S5. LOS standard deviation over the Afar region between November 2014 and August 2019 from Sentinel-1 tracks T087A, T014A, T116A, T079D, and T006D. Colour scale is limited to 5 mm to highlight variation in regions of low variance. Maximum standard deviation for each track is (2 s.f.): 15 mm/yr (T087A), 13 mm/yr (T014A), 3.2 mm/yr (T116A), 3.8 mm/yr (T079D), 3.1 mm/yr (T006D).

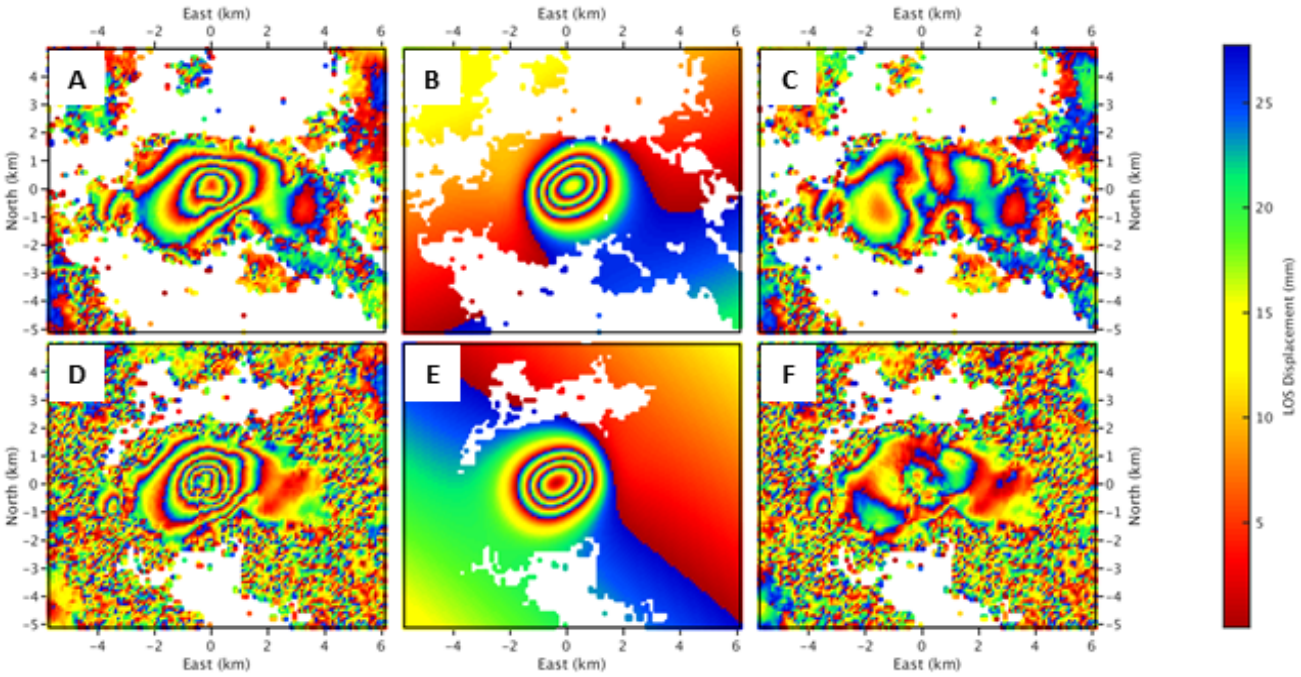

Figure S6. Sentinel-1 data (A,D), GBIS (Bagnardi & Hooper, 2018) model (B,E), and residual (C,F), for 2015-19 surface deformation observed using tracks T079D (A,B,C), and T014A (D,E,F) at Dallol volcano. Surface displacements are shown wrapped where each fringe (red-blue) represents 26 mm of motion towards the satellite in the line of sight. The model consists of a $\sim 1{\times}2$ km horizontal sill (Okada, 1985) at 0.9-1.3 km depth with ~ 0.27 m of contraction. The coordinate system is relative to the centre of the Dallol edifice.

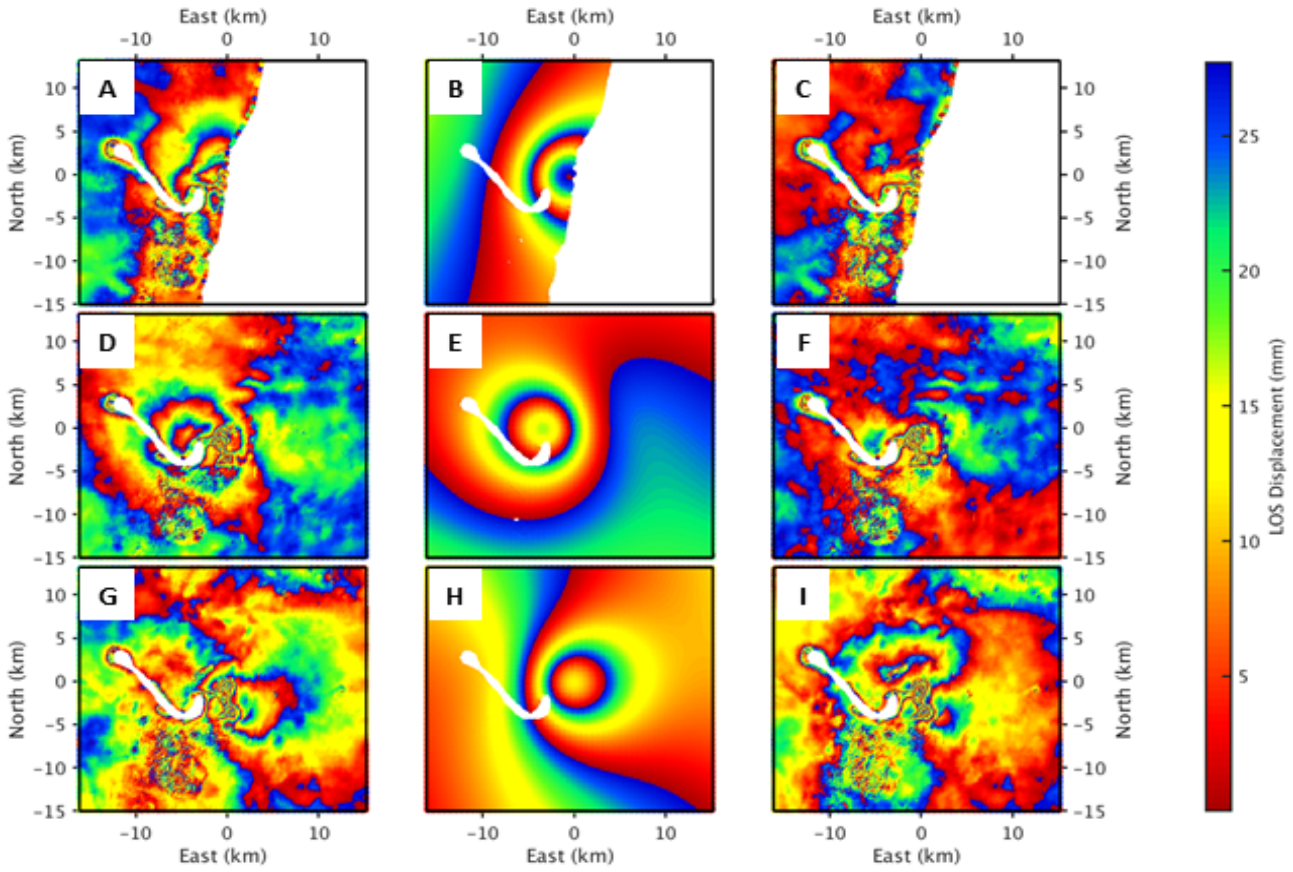

Figure S7. Sentinel-1 data (A,D,G), GBIS (Bagnardi & Hooper, 2018) model (B,E,H), and residual (C,F,I), for 2014-19 surface deformation observed using tracks T079D (A,B,C), T014A (D,E,F), and T006D (G,H,I) at Nabro volcano. Surface displacements are shown wrapped where each fringe (red-blue) represents 26 mm of motion towards the satellite in the line of sight. The model consists of a point source (Mogi, 1958) at 5.5-6.8 km depth with an equivalent volume change of 7-11$\times 10^6$ m^3. The coordinate system is relative to the centre of the Nabro edifice.